Inorganic Chemistry
Cite This: Inorg. Chem. 2019, 58, 9175−9180
Article
pubs.acs.org/IC

Organometallic-Derived Carbon (ODC)−Metal Nano-Oxide Composites as Improved Electrode Materials for Supercapacitors

Daniel Arenas-Esteban,*[,†] Esteban Urones-Garrote,[‡] Javier Carretero-González,[§] Viola Birss,[∥] L. Carlos Otero-Díaz,[†] and David Ávila-Brande*[,†]

[†]Department of Inorganic Chemistry, Faculty of Chemistry, Universidad Complutense de Madrid, Ciudad Universitaria 28040, Spain

[‡]National Center of Electron Microscopy, Universidad Complutense, E-28040 Madrid, Spain

[§]Institute of Polymer Science and Technology, ICTP-CSIC, Calle Juan de la Cierva 3, 28006 Madrid, Spain

[∥]Department of Chemistry, University of Calgary, Calgary, Alberta T2N 1N4, Canada

Supporting Information

ABSTRACT: In the search for the new generation of electrochemical energy storage materials, a novel and straightforward synthetic route for porous carbons and metal oxide nanoparticle composites based on the chlorination of the organometallic compounds $Ni(C_5H_5)_2$ and $Mn(C_5H_7O_2)_2$ at moderate temperatures, followed by hydrothermal treatment, has been developed. Electrochemical measurements in a three-electrode configuration show that, in both composites NiO@ODC and Mn_3O_4@ODC, a synergistic effect between the capacitive and pseudocapacitive energy storage mechanisms is observed, thereby improving their electrochemical performance vs pure carbon materials. Electrochemical evaluation of symmetric cells gave gravimetric capacitances of 124 and 130 F g^{-1} for NiO@ODC and Mn_3O_4@ODC, respectively. However, the porous structure of the carbon matrix and the higher conductivity of Mn_3O_4, together, were found to be responsible for the superior electrochemical performance of Mn_3O_4@ODC.

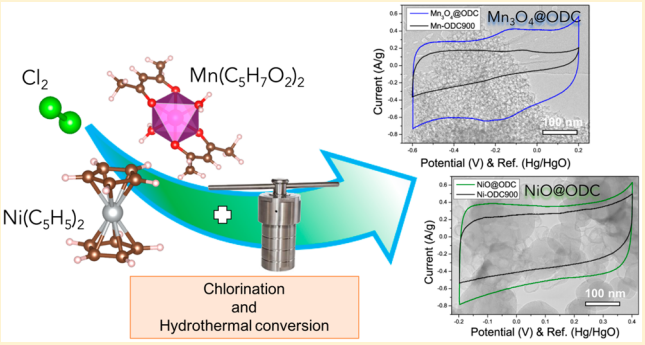

1. INTRODUCTION

Supercapacitors and batteries have attracted much interest in the last few decades due to the increase in energy consumption together with the depletion of conventional resources, based on fossil fuels, and the effect that their overuse has on climate change.[1]

Efforts have been focused especially on the development of electrochemical energy storage systems that should meet market requirements such as low cost, efficiency, and safety.[2]

In the particular case of supercapacitors, many materials such as porous carbon, transition-metal oxides, and conducting polymers have been tested as electrodes.[3]

Pseudocapacitive transition-metal oxide nanoparticles, such as NiO[4,5] and manganese oxides (MnO_x),[6] are promising candidates as electrodes due to their high specific capacitance, low cost, abundance, safety, and environmentally benign nature. Nonetheless, these excellent properties are limited by their poor electrical conductivity, cycling stability, and rate capability. In contrast, although carbon-based materials exhibit superior electrical conductivity, long cycle life, and high power density, their lower specific capacitance is unsatisfactory for practical applications where high energy density is required. Consequently, new electrode architectures based on the combinations of the previous materials can couple the advantages of each component in a single electrode.[7,8]

For these reasons, especially to further enhance their energy density without the sacrifice of power density, carbon-incorporated high-energy electrode materials, such as transition-metal oxides, have been developed. The main benefit of these composites is not only the presence of two active materials but also the improvement of the electrical conductivity and the mechanical strength in the composite. The success of this approximation hinges on the development of synthetic methods to load and/or incorporate these metal oxide nanoparticles within the carbon matrix. Most of the proposed routes can be divided into two concepts: either the deposition of the metal oxide nanoparticles on existing carbons (electrodeposition,[9] ultracentrifugation,[10] or atomic layer deposition[11] among others) or the cosynthesis of the carbon and the metal oxide components during the synthetic procedure, for example by conversion of a precursor material into carbon−metal oxide composite by carbonization[12] or vapor deposition[13] or by using wet-chemical approaches, such

Received: March 20, 2019
Published: July 1, 2019

DOI: 10.1021/acs.inorgchem.9b00800
Inorg. Chem. 2019, 58, 9175−9180

as sol−gel[14] or liquid-crystalline phase-templating methods.[15] Since these methods should prevent the blockage of the micropores of the carbon component and therefore both energy storage mechanisms can cooperate synergistically, the development of new synthetic routes to produce high-surface-area nanocomposites, avoiding a postactivation step, could help to produce electrode materials with improved electrochemical performances.

Chlorination of organometallic complexes, such as ferrocene, cobaltocene, and chromocene among others, has been described as a facile technique to produce low graphitizing carbon materials that are only mildly graphitized and have unique shapes, called organometallic-derived carbons (ODCs). These, consisting of highly disordered graphene-like layers and surface areas up to 1760 m^2/g,[16−18] have a pore size distribution mostly in the microporous region. During the chlorination reaction, metal halides are formed in the gas phase as secondary products. When the formed metal halide is highly volatile and the chlorination temperature is high enough, halides are easily eliminated from the carbon networks,[19] but if the metal halide has a higher boiling point or the chlorination temperature is not high enough, the metal halide formed cannot escape out of the ODC matrix, producing a composite material consisting of a carbon matrix containing a fine dispersion of metal halide nanoparticles.[20−22]

To take advantage of these subproducts of the chlorination reaction at low temperatures, in this work we describe the hydrothermal transformation of those halide nanoparticles into the corresponding stable electroactive nanooxides. The direct carbonization of metal−organic frameworks[23,24] and hydrothermal carbons impregnated with organometallic compounds[25] have been reported as new strategies to prepare carbon-based composites containing high amounts of metal or metal oxide nanoparticles with interesting electrochemical performances; however, these strategies involve not only the carbonization step but also previous stages, more than two, to synthesize the precursors for pyrolysis and many reagents are consumed. In this sense, our synthetic process seems less time-consuming and less costly.

Since NiO and MnO_x are promising candidates for active electrode materials in supercapacitors, in this paper we have employed nickelocene, $Ni(C_5H_5)_2$, and manganese(II) acetylacetonate, $Mn(C_5H_7O_2)_2$, as precursors for the formation of carbon−oxide nanocomposites. This is because they contain the carbon source and the metal part of the nanooxide directly linked in the same molecule. The morphology, nanostructure, and chemical composition of the materials were analyzed by electron microscopy and associated techniques. Nitrogen adsorption measurements were made to evaluate their textural properties, and finally electrochemical studies showed that the composite materials exhibited capacitance superior to that seen for the pure carbon materials, proposed to be due to the synergy between the two different storage mechanisms of the carbon and metal oxide components.

2. EXPERIMENTAL SECTION

2.1. Materials Preparation. In a first step, powder precursors $Ni(C_5H_5)_2$ and manganese(II) acetylacetonate $Mn(C_5H_7O_2)_2$ (Alfa Aesar, 99%) were placed in a quartz vessel and heated in a tubular furnace at 600 and 700 °C, respectively, as the final temperatures, with a heating rate of 50 °C/min. A continuous flow of high-purity chlorine gas (25 cm^3/min) was inserted while the reactor temperature was increased. When the final temperature was reached, the reaction time was set at 1 h. Excess chlorine and volatile metal halides were removed at the exit of the reactor and neutralized with a NaOH saturated solution. At the end of the reaction time, the chlorine gas flow was stopped and replaced with argon (25 cm^3/min) for the removal of the rest of the reacting chlorine and halides during the reactor cooling to room temperature by natural convection. The possible chlorination reactions can be described as follows:

$$Ni(C_5H_5)_2(s) + 6Cl_2(g) \rightarrow 10C(s) + NiCl_2(g) + 10HCl(g) \quad (1)$$

$$Mn(C_5H_7O_2)_2(s) + 4Cl_2(g) \rightarrow 10C(s) + MnCl_2(g) + 6HCl(g) + 4H_2O(g) \quad (2)$$

As the boiling points of $NiCl_2$ and $MnCl_2$ are 985 and 1190 °C, respectively, well below the chlorination temperature, we expected to obtain either a mixture of carbon and metal halides or a carbon-based composite containing metal halide nanoparticles. In order to demonstrate the improvement of the electrochemical performances in the composites, pure ODCs from both precursors were synthesized following the same procedure but reaching a chlorination temperature of 900 °C.

Then, the chlorinated materials at 600 and 700 °C were placed in a hydrothermal Teflon/stainless steel chamber containing 30 mL of 12 M KOH. The autoclave was heated at 200 °C for 48 h, and then the samples were filtered under vacuum and washed with abundant water and the residual black powders were dried at 100 °C overnight.

2.2. Materials Characterization. Conventional transmission electron microscopy (TEM) experiments were performed on a JEOL 2100 (acceleration voltage of 200 kV) microscope (point resolution of 0.25 nm), whereas high-resolution TEM and high-angle annular dark field scanning-TEM (HAADF-STEM) studies were performed with a JEOL 3000 F (acceleration voltage of 300 kV) microscope (point resolution of 0.17 nm).

Thermogravimetric analysis (TGA) was performed on a TA Instruments apparatus (SDT Q600 model) using an O_2 atmosphere. The sample was heated at 5 °C min^{-1} up to 900 °C.

The surface area and pore structure characterizations were made by means of N_2 adsorption−desorption isotherms at 77 K using a surface area and porosity analyzer (Micromeritics ASAP 2020). The specific surface areas (S_{BET}) were determined according to BET theory, and the pore size distributions (PSDs) were calculated using the SAEIUS software for the 2D nonlocal density functional theory (2D-NLDFT) by considering the pore walls of the standard carbon slit-shaped pore geometry to be energetically heterogeneous.[26,27]

2.3. Electrochemical Measurements. The electrochemical characterization was evaluated in a first step by cyclic voltammetry in a three-electrode cell, containing a deaerated 1 M NaOH aqueous electrolyte solution, a platinized Pt mesh as the counter electrode (CE), Hg/HgO as the reference electrode (ref), and a glassy-carbon (GC) rod (ø = 0.7 cm) as the working electrode (WE). The carbon material was in powder form (0.01 g), dispersed in 0.4 g of a 1 wt % Nafion/ethanol solution, and the mixture was then sonicated for at least 30 min to obtain a carbon/Nafion ink. This ink (11 μL) was deposited on the surface of the WE and dried at room temperature to form a carbon film.

In order to better compare the response as a function of sweep rate, the current response was normalized to sweep rate. Afterward, the capacitive performance of the materials was measured in a two-electrode symmetrical configuration Swagelok-type cell. Disk-shaped electrodes were prepared by mixing 95 wt % of the carbon material (typically 0.05 g) with 5 wt % of a polytetrafluoroethylene aqueous solution (PTFE 60 wt %, Sigma-Aldrich) as the polymer binder (0.0044 g). The mixture was hand-mixed with a few milliliters of ethanol until a viscous slurry was obtained. The slurry was laminated with the help of a glass test tube until the final thickness was within the 250−200 μm range. Then, the film was dried and kept at 120 °C under vacuum for 12 h prior to each measurement.

Electrodes of comparable mass and 10 mm in diameter were assembled in the symmetrical Swagelok-type cell, wetted with the

DOI: 10.1021/acs.inorgchem.9b00800
Inorg. Chem. 2019, 58, 9175−9180

electrolyte, separated with a glass fiber membrane (Whatman glass microfiber filters, grade GF/B) of 12.7 mm in diameter, and placed in direct contact with titanium plungers. Electrochemical studies were performed in a 1 M aqueous solution of NaOH in a voltage window ranging from 0 to 1 V. Galvanostatic measurements from 0.1 to 10 A g^{-1} were performed under ambient conditions with a multichannel potentiostat/galvanostat (Biologic VMP3, France). The specific capacitance was evaluated per active mass of a single electrode. Pulsed electrochemical impedance spectroscopy (PEIS) measurements were performed by applying a low sinusoidal amplitude alternating voltage of 10 mV to the cell at frequencies ranging from 1 MHz to 10 mHz using the aforementioned multichannel potentiostat/galvanostat. Measurements were performed at open circuit voltage (OCV).

The specific capacitance (C_{grav}) for the two-electrode cell was calculated from the galvanostatic charge−discharge plot, using the equation

$$C_{grav} = \frac{2It}{m_e \Delta E_{cell}} \quad (3)$$

where I (A) is the current, m (g) refers to the mass of active material in a single electrode, t (s)/ΔE_{cell} (V) is the inverse of the slope extracted from the galvanostatic discharge curve after ohmic drop subtraction. and V is the cell potential. The volumetric capacitance was calculated by considering the density of a single electrode including the polymer binder fraction.

3. RESULTS AND DISCUSSION

3.1. Structural Characterizations of the Composites NiO@ODC and MnO_x@ODC. The synthetic pathway followed to produce the nanocomposites NiO@ODC and MnO_x@ODC is graphically depicted in Figure 1.

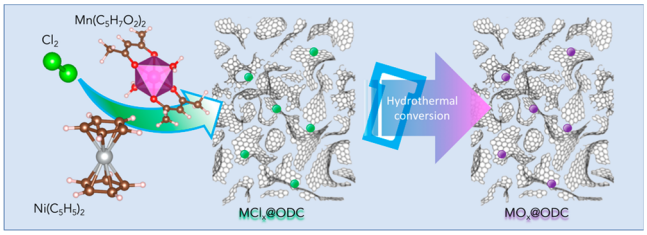

Figure 1. Schematic illustration of the chemical synthesis in which the organometallic precursors are initially transformed into the composites $NiCl_2$@ODC and $MnCl_2$@ODC by a partial chlorination etching and subsequently hydrothermally converted into the composites NiO@ODC and MnO_x@ODC.

The success of the procedure has been confirmed by transmission electron microscopy, since X-ray diffraction patterns only show the typical pattern of disordered materials, suggesting the presence of ultrafine nanoparticles imbibed in the disordered carbon matrix (see Figure S1). In the low-magnification TEM images displayed in Figure 2, we can observe the morphological features of the organometallic precursors after chlorination. The material obtained from $Mn(C_5H_7O_2)_2$ (see Figure 2a) is composed of highly entangled and corrugated carbon foils, whereas the chlorination of $Ni(C_5H_5)_2$ (see Figure 2d) yields solid spheres (diameter from 70 to 170 nm) and small hollow spheres (diameter from 40 to 55 nm and wall thickness from 5 to 12 nm) that seem to be decorating the surface of the solid spheres. In some cases, these hollow spheres look open or broken.

The presence of a homogeneous contrast indicates that these materials apparently do not contain large imbibed metal

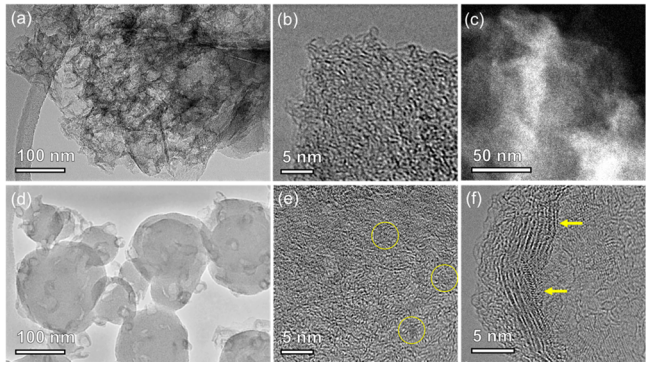

Figure 2. (a) Low-magnification TEM image and (b) high-resolution TEM image of $MnCl_2$@ODC composite. (c) HAADF-STEM image of the $MnCl_2$@ODC composite where the manganese chloride nanoparticles are detected as the brightest contrast areas. (d) Low-magnification TEM image and (e, f) high-resolution TEM images of $NiCl_2$@ODC composite recorded near the edge of the solid and hollow spheres, respectively, where $NiCl_2$ nanoparticles can be identified by yellow circles and arrows.

halide nanocrystals. However, the EDS (energy dispersive spectroscopy) analyses in several areas of the materials detected the presence of Mn, Ni, and Cl, suggesting the presence of small nanocrystals of $MnCl_2$ and $NiCl_2$ within the carbon matrix.

A closer inspection at higher magnifications was performed by HRTEM at the edge of the material prepared with $Mn(C_5H_7O_2)_2$ (see Figure 2b), revealing a contrast characteristic of highly disordered carbon materials, where the graphene-like layers are randomly stacked and surround darker dots smaller than 1 nm in size. These correspond to the $MnCl_2$-embedded nanocrystals. The presence of these nanocrystals is more evident in the Z-contrast image taken at the edge of a particle, where the brighter contrast corresponds to areas enriched in $MnCl_2$ nanocrystals (see Figure 2c).

The HRTEM images recorded at the edges of the solid and hollow spheres, formed after chlorination of $Ni(C_5H_5)_2$ (Figure 2e,f, respectively) show that both nanostructures are formed by disordered graphene-like layers containing a good dispersion of imbedded $NiCl_2$ nanocrystals larger than 1 nm. The formation of these composites as an intermediate product in the preparation of the organometallic-derived carbons (ODC) suggests the possibility of the transformation of $MnCl_2$ and $NiCl_2$ into MnO_x and NiO nanoparticles, yielding the new composite materials (MnO_x@ODC and NiO@ODC) containing the electroactive nano-oxides.

After chlorination, the oxidation step is performed at low temperatures (200 °C) by hydrothermal treatment of the intermediate composite in basic media, converting the metal halide nanoparticles into the nano-oxides without affecting the carbon matrix nanostructure. The conventional TEM images at low magnifications displayed in Figure 3a,d confirm that the morphology of the materials is retained after oxidation. The differences in contrast detected in the low-magnification high angle annular dark field (HAADF) images (Figure 3b,e) confirm that both materials are composed of a matrix of a low-atomic-weight element containing brighter areas of a heavier element.

A closer inspection demonstrates that the bright areas consist of well-dispersed nanoparticles in the range of 5−30 nm. The nanoparticles are identified as hausmannite-type

DOI: 10.1021/acs.inorgchem.9b00800
Inorg. Chem. 2019, 58, 9175−9180

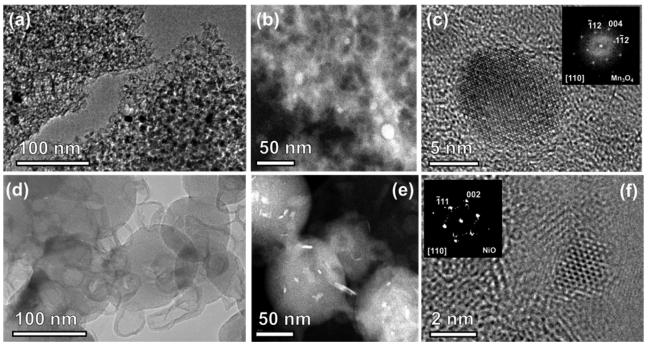

Figure 3. (a) Low-magnification TEM image, (b) HAADF-STEM image, and (c) high-resolution TEM image showing a single nanoparticle identified as a Mn_3O_4 nanoparticle of the Mn_3O_4@ODC composite material. (d) Low-magnification TEM image (e) HAADF-STEM image, and (f) high-resolution TEM image showing a single nanoparticle identified as a NiO nanoparticle of the NiO@ODC composite material.

Mn_3O_4 nanocrystals oriented along the [110] zone axis in the HRTEM image displayed in Figure 3c. In a similar way, in Figure 3f, a nanocrystal identified as NiO, oriented along the [110] zone axis, is seen to be assembled well within the carbon matrix.

The amount of metal nanooxides in the composites has been analyzed by thermogravimetric analysis of a portion of NiO@ODC and Mn_3O_4@ODC in air (see Figure S2), yielding losses of carbon of 83 and 97% and therefore a content of NiO of 17% and that of Mn_3O_4 nanoparticles of 3%.

3.2. Textural Characterization. The textural parameters (surface area, pore size distribution) were obtained from the N_2 adsorption–desorption measurements performed on the Mn_3O_4@ODC and NiO@ODC composite materials.

The isotherm plots (Figure 4a) can be considered as type I, related to microporous materials, according to the IUPAC

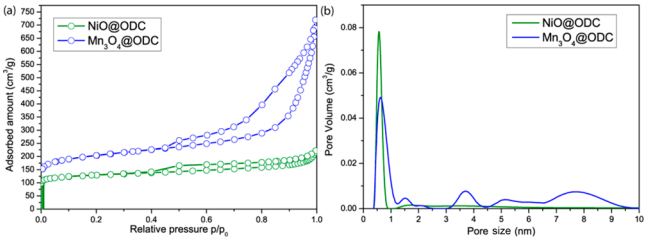

Figure 4. (a) Comparison of the standard nitrogen adsorption–desorption isotherms at 77 K for Mn_3O_4@ODC and NiO@ODC. (b) Representation of the pore size distributions showing the region with pore width up to 10 nm.

classification.[28] The isotherms also exhibit a wide H4 hysteresis loop,[29] which is associated with the presence of mesopores. In the case of NiO@ODC, the thinner hysteresis loop can indicate the presence of small amount of mesopores, whereas the larger loop, exhibited by Mn_3O_4@ODC, is associated with an important contribution of mesopores. Notably, a significant amount of nitrogen is seen to be adsorbed at relative pressures of $p/p^0 > 0.7$, revealing the existence of textural porosity, originated by the formation of voids between the composite particles. Results derived from the assessment of the surface area values are collected in Table 1. The specific surface areas, obtained using the BET theory, are 749 and 422 m^2/g for

Table 1. Textural Parameters Extracted for NiO@ODC and Mn_3O_4@ODC

	$S_{BET\ total}$ (m^2/g)	S_{ext} (m^2/g)	S_{mic} (m^2/g)
NiO@ODC	422	80	341
Mn_3O_4@ODC	749	465	284

Mn_3O_4@ODC and NiO@ODC, respectively. The largest surface area found in Mn_3O_4@ODC is in agreement with the fact that this material is built up by a low-density carbon matrix composed of entangled and corrugated foils, whereas the presence of large amounts of solid spheres in NiO@ODC could be responsible for its lower surface area.

The pore size distribution (PSD) plots, derived from the NLDFT method, are depicted in Figure 4b. The plot in the case of NiO@ODC confirms the development of narrow micropores (pore width of 0.56 nm). However, the plot for the ODC@Mn_3O_4 material reveals a more complex pore structure containing narrow (pore width 0.62 nm) and wider (pore width 1.48 nm) microporosity, as well as some mesopores ranging from 3 to 10 nm in diameter (Table 1). In this sense, mesoporosity in this material can be attributed to pores formed between the corrugated carbon foils detected by the TEM study (Figure 3).

3.3. Electrochemical Characterization. Both nanoparticle composite electrodes were first tested by cyclic voltammetry (CV) by using a three-electrode cell configuration and then also compared with their respective carbon analogues without any metal nanoparticles present. These were removed after chlorination of the organometallic precursor at 900 °C (see Figure S3). The composite electrode materials exhibited higher gravimetric capacitance values than their respective carbon material analogues (see Figure S4a,b). Additionally, in the CVs of the composite electrodes, by considering that during the voltammetry experiment the current response for each sweep rate varies depending on whether the redox process is diffusion-controlled or surface-controlled (capacitive), both contributions can be discriminated and estimated[30](see Figure S4c,d).

The CV of the NiO@ODCmaterial at 5 mV s^{-1} (Figure 5a) exhibited a quasi-rectangular shape corresponding to a typically

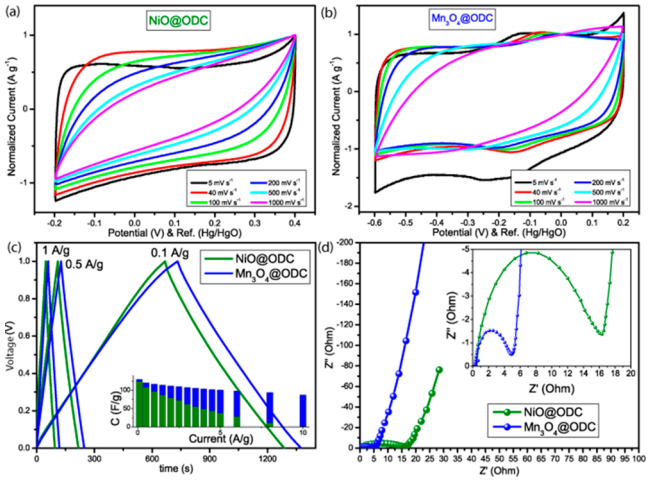

Figure 5. Normalized current CVs in a three-electrode cell of (a) NiO@ODC and (b) Mn_3O_4@ODC at increasing sweep rates from 5 to 1000 mV s^{-1}. (c) GCPL and (d) EIS on Nyquist plots of both composite materials.

DOI: 10.1021/acs.inorgchem.9b00800
Inorg. Chem. 2019, 58, 9175–9180

capacitive behavior. In contrast, the CV for the Mn_3O_4@ODC (Figure 5b) at the same sweep rate shows both a capacitive feature along with a peak, centered at −0.12 V, most likely corresponding to a Faradaic process. In the case of the Mn_3O_4@ODC composite, the reversible redox process could arise from the intercalation-type pseudocapacitance (bulk) of the Mn_3O_4 nanoparticles during charge/discharge, in contrast to the surface-type pseudocapacitance associated with the oxidation reduction of the NiO nanoparticle surfaces present in the NiO@ODC material, which take place through the entire potential window.[31]

As the sweep rate was increased, the CV for the NiO@ODC composite material begins to lose its quasi-rectangular shape, becoming more tilted, likely due to some transport limitations within the material. However, in the CVs of the Mn_3O_4@ODC composite, the quasi-rectangular shape was retained up to 200 mV s^{-1}, indicating a better pore structure that allows for faster ion diffusion. The narrow micropore size evidenced for the NiO@ODC composites may then be limiting ion diffusion during charge/discharge, while in the Mn_3O_4@ODC material, ion transport is facilitated by the presence of a mesopore distribution between 2 and 10 nm in size (see Table 1).

The promising electrochemical properties exhibited by these novel composite electrode materials were also seen in the results obtained using a two-electrode cell configuration. The potential window stability of the composite electrodes (see Figure S5) has been previously tested by recording CVs from 0 up to 1 V. Figure 5c shows the galvanostatic charge−discharge curves of both supercapacitor composites at 0.1, 0.5, and 1 A g^{-1} and the gravimetric capacitance calculated from their integral up to 10 A g^{-1}. The gravimetric capacitance value calculated for Mn_3O_4@ODC was 130 F g^{-1}, and the value for the NiO@ODC electrode was 124 F g^{-1}, similar to capacitance values reported for other carbon−metal oxide composites.[32,33] As was already discussed above for the CV results, the degrees of retention of the capacitance were both composites was very different. While the NiO@ODC system quickly lost all of its capacitance at 10 A g^{-1}, the Mn_3O_4@ODC retained up to 67% at the same current. This is again likely due to the more desirable pore structure of the ODC@Mn_3O_4 material in comparison to the NiO@ODC composite.

A Nyquist plot (Figure 5d), obtained from impedance measurements, allowed for the calculation of the equivalent series resistance (ESR) value for the two electrode materials. While NiO@ODC showed a resistive behavior with an ESR value of 17 Ω, the Mn_3O_4@ODC composite exhibits a significantly lower ESR value of 4.6 Ω, improving the relaxation time constant calculated from the complex impedance data by 1 order of magnitude, from 29 to 2.9 s (see Figure S6). The superior electrical conductivity of Mn_3O_4 (1.6×10^{-2} S cm^{-1} [32]) in comparison to NiO (10^{-13} S cm^{-1} [34]) nanoparticles also contributes to the decrease in the ESR value of the Mn_3O_4@ODC composite. Overall, this material is thus a very promising starting point to be optimized in the search of future electrodes in supercapacitive devices. The energy density calculated for the symmetric cells of NiO@ODC and Mn_3O_4@ODC are 4.3 and 4.7 Wh/kg, respectively. These values are below the reported for active carbons in commercial supercapacitors exhibiting an energy density of 24.8 Wh/kg,[35] since our measurements in aqueous electrolytes are limited to a narrower voltage window (1 V) in comparison to that of organic electrolytes (2.8 V) used in the assembly of commercial supercapacitors.

4. CONCLUSIONS

Micro- and mesoporous carbons, containing a fine dispersion of either NiO or Mn_3O_4 nanoparticles, have been synthesized by using a novel and straightforward synthetic route. This was based on the chlorination of $Ni(C_5H_5)_2$ and $Mn(C_5H_7O_2)_2$ at intermediate temperatures, followed by the hydrothermal conversion of the byproduct, composed of $NiCl_2$ and $MnCl_2$ nanoparticles embedded in the carbon matrix, into the target composites, NiO@ODC and Mn_3O_4@ODC. The success of the proposed procedure has been demonstrated by imaging of the NiO@ODC and Mn_3O_4@ODC composites and their respective intermediates, $NiCl_2$@ODC and $MnCl_2$@ODC, by transmission electron microscopy. This revealed the retention of the shape and microstructure of the carbon matrix, consisting of highly entangled and corrugated carbon foils and large solid spheres, decorated with smaller hollow spheres.

Electrochemical studies in a three-electrode configuration demonstrated an improvement in the electrochemical properties of these new composites in comparison with the porous carbons obtained by chlorination of the precursors at 900 °C. In addition, the differences in the microstructure of the carbon component, the porous architecture developed, and the better electronic conductivity of Mn_3O_4 are the likely reasons for the superior electrochemical performance of Mn_3O_4@ODC in the symmetrical cell.

The present work has clearly shown that, depending on the nature of the organic ligand linked to the metal of the organometallic precursor, the final microstructure and the textural properties of the carbon component vary significantly. Therefore, since the number of possible organometallic precursors is extremely large and many of them are commercially available, the present results are very promising. This is because this method could lead to the synthesis of a wide range of porous carbon@metal oxide nanoparticle composites for use in the next generation of electrode materials for electrochemical energy storage applications.

■ ASSOCIATED CONTENT

Supporting Information

The Supporting Information is available free of charge on the ACS Publications website at DOI: 10.1021/acs.inorgchem.9b00800.

Additional figures as described in the text (PDF)

■ AUTHOR INFORMATION

Corresponding Authors

*E-mail for D.A.-E.: darenas@ucm.es.
*E-mail for D.A.-B.: davilabr@ucm.es.

ORCID

Javier Carretero-González: 0000-0002-8008-5715
David Ávila-Brande: 0000-0003-0452-2482

Notes

The authors declare no competing financial interest.

■ ACKNOWLEDGMENTS

The authors acknowledge financial support through the Comunidad de Madrid Project S2013/MIT-2753 (MATERYENER-3) and the Retos Projects from MINECO with references MAT2017-86796-R and MAT2017-84385-R. J.C.-G, thanks the Spanish Ministry of Economy, Industry and

DOI: 10.1021/acs.inorgchem.9b00800
Inorg. Chem. 2019, 58, 9175−9180

Competitiveness, for funding through a Ramón y Cajal fellowship (RYC-2015-01627).

REFERENCES

(1) World Energy Council. *World Energy Issues Monitor-Managing the Grand Energy Transition*, 2019.
(2) Armand, M.; Tarascon, J. M. Building better batteries. *Nature* **2008**, *451*, 652−657.
(3) Chen, X.; Paul, R.; Dai, L. Carbon-based supercapacitors for efficient energy storage. *Natl. Sci. Rev.* **2017**, *4*, 453−489.
(4) Zhu, Y.; Cao, C.; Tao, S.; Chu, W.; Wu, Z.; Li, Y. Ultrathin Nickel Hydroxide and Oxide Nanosheets: Synthesis, Characterizations and Excellent Supercapacitor Performances. *Sci. Rep.* **2015**, *4*, 5787.
(5) Chen, F.; Zhou, W.; Yao, H.; Fan, P.; Yang, J.; Fei, Z.; Zhong, M. Self-assembly of NiO nanoparticles in lignin-derived mesoporous carbons for supercapacitor applications. *Green Chem.* **2013**, *15*, 3057−3063.
(6) Toupin, M.; Brousse, T.; Bélanger, D. Charge Storage Mechanism of MnO2 Electrode Used in Aqueous Electrochemical Capacitor. *Chem. Mater.* **2004**, *16*, 3184−3190.
(7) Yu, Z.; Tetard, L.; Zhai, L.; Thomas, J. Supercapacitor electrode materials: nanostructures from 0 to 3 dimensions. *Energy Environ. Sci.* **2015**, *8*, 702−730.
(8) Jiang, H.; See-Lee, P.; Li, C. 3D-carbon based nanostructures for advanced supercapacitors. *Energy Environ. Sci.* **2013**, *6*, 41−53.
(9) Ren, Y.; Sun, C.; Song, M.; Wang, L. Preparation of Porous Carbon-Manganese Dioxide Nanocomposite as a Supercapacitor Electrode. *Int. J. Electrochem. Sci.* **2016**, *11*, 10706−10714.
(10) Iwama, E.; Simon, P.; Naoi, K. Ultracentrifugation: An effective novel route to ultrafast nanomaterials for hybrid supercapacitors. *Curr. Opin. Electrochem.* **2017**, *6*, 120−126.
(11) George, S. M. Atomic layer deposition: an overview. *Chem. Rev.* **2010**, *110*, 111−31.
(12) Meng, W.; Chen, W.; Zhao, L.; Huang, Y.; Zhu, M.; Huang, Y.; Fu, Y.; Geng, F.; Yu, J.; Chen, X.; Zhi, C. Porous Fe_3O_4/carbon composite electrode material prepared from metal-organic framework template and effect of temperature on its capacitance. *Nano Energy* **2014**, *8*, 133−140.
(13) Wang, X.; Yushin, G. Chemical vapor deposition and atomic layer deposition for advanced lithium ion batteries and supercapacitors. *Energy Environ. Sci.* **2015**, *8*, 1889−1904.
(14) Dhere, S. Electrode materials for supercapacitors synthesized by sol−gel process. *Curr. Sci.* **2018**, *115*, 436−449.
(15) Yu, C.; Tian, B.; Zhao, D. Recent advances in the synthesis of non-siliceous mesoporous materials. *Curr. Opin. Solid State Mater. Sci.* **2003**, *7*, 191−197.
(16) Ayape-Katcho, A.; Urones-Garrote, E.; Ávila-Brande, D.; Gómez-Herrero, A.; Urbonaite, S.; Csillag, S.; Lomba, E.; Agulló-Rueda, F.; Landa-Cánovas, A. R.; Otero-Díaz, L. C. Carbon Hollow Nanospheres from Chlorination of Ferrocene. *Chem. Mater.* **2007**, *19*, 2304−2309.
(17) Urones-Garrote, E.; Ávila-Brande, D.; Ayape-Katcho, N.; Gómez-Herrero, A.; Landa-Cánovas, A. R.; Lomba, E.; Otero-Díaz, L. C. Spherical carbon nanoparticles produced by direct chlorination of cobaltocene. *Carbon* **2007**, *45*, 1699−1701.
(18) González-García, P.; Urones-Garrote, E.; Ávila-Brande, D.; Otero-Díaz, L. C. Carbon particles of variable shape produced by the chlorination of bis(benzene)chromium. *J. Organomet. Chem.* **2013**, *740*, 141−147.
(19) González-García, P.; Centeno, T. A.; Urones-Garrote, E.; Ávila-Brande, D.; Otero-Díaz, L. C. Porous carbon nanospheres derived from chlorination of bis(cyclopentadienyl)titanium dichloride and their electrochemical capacitor performance. *Mater. Chem. Phys.* **2011**, *130*, 243−250.
(20) Urones-Garrote, E.; Ávila-Brande, D.; Ayape-Katcho, N.; Gómez-Herrero, A.; Landa-Cánovas, A. R.; Otero-Díaz, L. C. Amorphous carbon nanostructures from chlorination of ferrocene. *Carbon* **2005**, *43*, 978−985.
(21) Urones-Garrote, E.; Gómez-Herrero, A.; Ávila-Brande, D.; Ayape-Katcho, N.; Lomba, E.; Landa-Cánovas, A. R.; Otero-Díaz, L. C. Transmission electron microscopy characterization of nanostructured carbon derived from Cr_3C_2 and $Cr(C_5H_7O_2)_3$. *Carbon* **2010**, *48*, 1425−1433.
(22) González-García, P.; Arenas-Esteban, D.; Ávila-Brande, D.; Urones-Garrote, E.; Otero-Díaz, L. C. Nickelocene as precursor of microporous organometallic-derived carbon and nickel oxide-carbon nanocomposite. *J. Colloid Interface Sci.* **2017**, *490*, 410−419.
(23) Wu, M.-S.; Wen-Hao, H. Nickel nanoparticles embedded in partially graphitic porous carbon fabricated by direct carbonization of nickel-organic framework for high-performance supercapacitors. *J. Power Sources* **2015**, *274*, 1055−1062.
(24) Zhao, K.; Lyu, K.; Liu, S.; Gan, Q.; He, Z.; Zhou, Z. Ordered porous Mn_3O_4@N-doped carbon/graphene hybrids derived from metal−organic frameworks for supercapacitor electrodes. *J. Mater. Sci.* **2017**, *52*, 446−457.
(25) Liu, T.; Liu, E.; Ding, R.; Luo, Z.; Hu, T.; Li, Z. Preparation and supercapacitive performance of clew-like porous nanocarbons derived from sucrose by catalytic graphitization. *Electrochim. Acta* **2015**, *173*, 50−58.
(26) Jagiello, J.; Olivier, J. P. 2D-NLDFT adsorption models for carbon slit-shaped pores with surface energetical heterogeneity and geometrical corrugation. *Carbon* **2013**, *55*, 70−80.
(27) Jagiello, J.; Olivier, J. P. Carbon slit pore model incorporating surface energeticalheterogeneity and geometrical corrugation. *Adsorption* **2013**, *19*, 777−783.
(28) Rouquerol, F.; Rouquerol, J.; Sing, K. S. W. *Adsorption by Powders and Porous Solids*; Academic Press: London, 1999.
(29) Sing, K. S. W. Reporting physisorption data for gas/solid systems with special reference to the determination of surface area and porosity. *Pure Appl. Chem.* **1985**, *57*, 603−619.
(30) Augustyn, V.; Simon, P.; Dunn, B. Pseudocapacitive oxide materials for high-rate electrochemical energy storage. *Energy Environ. Sci.* **2014**, *7* (5), 1597−1614.
(31) Lukatskaya, M. R.; Dunn, B.; Gogotsi, Y. Multidimensional materials and device architectures for future hybrid energy storage. *Nat. Commun.* **2016**, *7*, 12647.
(32) Lota, K.; Sierczynska, A.; Lota, G. Supercapacitors Based on Nickel Oxide/Carbon Materials Composites. *Int. J. Electrochem.* **2011**, *2011*, 321473.
(33) Dubal, D. P.; Dhawale, D. S.; Salunkhe, R. R.; Fulari, V. J.; Lokhande, C. D. Chemical synthesis and characterization of Mn_3O_4 thin films for supercapacitor application. *J. Alloys Compd.* **2010**, *497*, 166−170.
(34) Siddique, M. N.; Ahmed, A.; Tripathi, P. Electric transport and enhanced dielectric permittivity in pure and Al doped NiO nanostructures. *J. Alloy. Comp.* **2018**, *735*, 516−529.
(35) Nishihara, H.; Simura, T.; Kobayashi, S.; Nomura, K.; Berenguer, R.; Ito, M.; Uchimura, M.; Iden, H.; Arihara, K.; Ohma, A.; Hayasaka, Y.; Kyotani, T. *Adv. Funct. Mater.* **2016**, *26*, 6418−6427.

DOI: 10.1021/acs.inorgchem.9b00800
Inorg. Chem. 2019, 58, 9175−9180